Design of prism coupling structure for liquid crystal cladding waveguide beam steerer

Zekun Bi,[1,2,3] **Quanquan Mu,**[1,2,3,*] **Zhihui Diao,**[1,2,3,4]
Yonggang Liu,[1,2,3] **Chengliang Yang,**[1,2,3] **Zenghui Peng,**[1,2,3]
Dayu Li,[1,2,3] **Weifang Fan,**[1,2,3] **and Yunhui Yu**[1,2,3]

[1] *State Key Laboratory of Applied Optics, Changchun Institute of Optics, Fine Mechanics and Physics, Chinese Academy of Sciences, Changchun 130033, China*
[2] *Key Laboratory of Optical System Advanced Manufacturing Technology, Chinese Academy of Sciences, Changchun 130033, China*
[3] *Center of Materials Science and Optoelectronics Engineering, University of Chinese Academy of Sciences, Beijing 10049, China*
[4] *diaozh@ciomp.ac.cn*
[*]muquanquan@ciomp.ac.cn

Abstract: This paper proposes an extended prism coupling analysis method to accurately analyze the coupling structure of liquid crystal (LC) cladding waveguide beam steerer. We analyze the effects of LC anisotropy on the coupling of transverse electric (TE) and transverse magnetic (TM) modes and derive the expression of the optical field distribution that perfectly matches the given coupling structure. Based on this method, we present the optimal coupling structure for Gaussian beam. Taking into account the practical manufacturing process, we propose a simplified coupling structure and perform a detailed analysis of its performance based on numerical simulations. Experimental results show a coupling efficiency of 91% and a coupling angle full width at half maximum (FWHM) of about ±0.02°, demonstrating the effectiveness of the proposed method in predicting the coupling performance of anisotropic cladding waveguides.

1. Introduction

Beam steering technology plays a pivotal role in various applications, including microscopy [1], light detection and ranging (LiDAR) [2,3], and projection displays [4]. Traditional mechanical beam steering method suffers from the drawbacks of large volume, high power consumption, limited pointing accuracy, etc. Over the past years, scholars from various countries have been exploring non-mechanical beam steering (NMBS) technology and have made much progress, such as acousto-optic deflectors [5,6], electro-wetting electrodes [7], liquid crystal optical phased arrays (LCOPAs) [8,9], and liquid crystal polarization gratings (LCPGs) [10,11]. Currently, achieving fast, large field-of-view and high-precision beam steering remains the core technical challenge faced by NMBS technology.

In 2015, Vescent Photonics [12] reported a Steerable Electro-Evanescent Optical Refractor (SEEOR), which achieved 50°×15° two-dimensional continuous beam steering at 1550 nm wavelength. This device is based on refraction, and overcomes the inherent limitations of diffraction efficiency that affect acousto-optic and LCOPAs devices as the scanning angle increases. It also provides large continuous angular coverage and eliminates the need for complicated stacks of small-angle and large-angle steerers as sometimes required by diffractive approaches. In addition, the device employs liquid crystal (LC) surface molecules for control and achieves a sub-millisecond response time. In 2018, Jesse A. Frantz et al. [13,14] further extended this technology to the mid-wave infrared. Figure 1(a) illustrates the cross-section of the SEEOR structure, which comprises a coupling prism, a common electrode layer, a gap layer, a core layer, an alignment layer, an LC layer, and a cover glass with driving electrode and alignment

layer. The SEEOR can be divided into three regions along the z axis: input coupling region, horizontal beam steering region, and output coupling region (vertical steering region). At the input coupling region ($0 \le z \le z_1$), the thickness distribution of the gap and core layers should be carefully designed for efficient coupling. At the horizontal beam steering area ($z_1 < z < z_2$), the thicknesses of the core and gap layer remain constant. The driving electrode at this region was divided into two parts by a zigzag pattern, as shown in Fig. 1(b). By applying different voltages to each part, the effective refractive index of the waveguide will change and because of the refractive phenomenon at each z-shaped interface, the propagating light will be steered, resulting in continuous beam steering in the y direction. The coupling output region ($z \ge z_2$) has the same structure as the input coupling region. By changing the voltage applied to the vertical steering electrode, as shown in Fig. 1(b), the beam can be steered in the x direction.
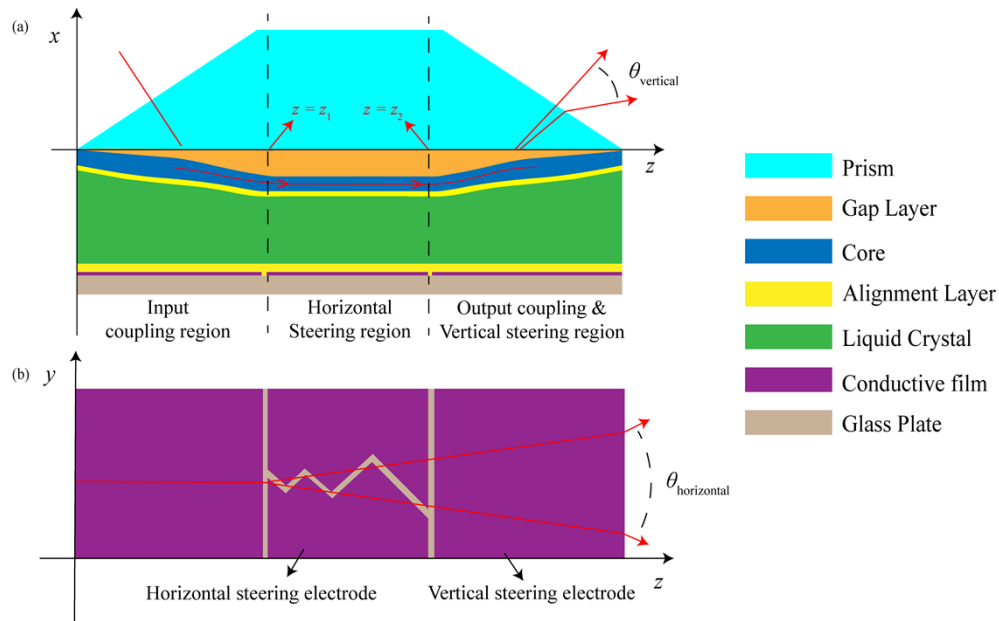

Fig. 1. (a) Cross sectional schematic diagram of SEEOR. (b) Patterned electrodes.

Due to the unique electric control characteristics of the LC cladding layer, this structure exhibits remarkable performance and developmental potential. However, the LC cladding exhibits anisotropic optical properties, which poses a challenge to the design and analysis of prism coupling structures. The coupling structure of SEEOR was based on the prism coupling principle, which was introduced by Ulrich. In order to analyze the coupling efficiency, Ulrich [15] established a coupling analysis model based on the weak coupling assumption. In 1981, J.F. Revelli [16] established an ideal beam function Ω^* to calculate the coupling efficiency under arbitrary coupling strength with inverse analysis and overlap integral procedure. By accurately solving the boundary value problem of the waveguide system, the prism coupling theory was extended to the strong coupling regime. Simulation results [17] showed that J.F. Revelli's theory had high consistency with Ulrich's theory in the weak coupling limit. However, both theories are based on isotropic cladding structures and cannot be directly used for LC cladding analysis.

On the basis of J.F. Revelli's theory, this paper proposes and establishes an extended prism coupling analysis method suitable for anisotropic cladding structure, theoretically studies the influence of anisotropic LC cladding on transverse electric (TE) and transverse magnetic (TM) mode coupling process. A reverse analysis method similar to J.F. Revelli's approach is employed

to obtain the field distribution Ω^* leaked from the waveguide to the prism by accurately solving the boundary value problem of the waveguide system and further gives the optimal design of prism coupling structure for Gaussian beam incidence. A simplified coupling structure with coupling efficiency over 94% was also proposed for the convenience of manufacturing. Finally, the preparation and performance testing of the device was completed.

2. Ω^* of SEEOR coupling structure

The input coupling structure was shown in Fig. 1(a), the relative permittivity tensor of the coupling prism, gap layer, core layer, alignment layer, and LC are ε_3, ε_2, ε_1, ε_0, and ε_{LC}, respectively. The thicknesses of the gap layer, core layer, and alignment layer are denoted as s (z), d (z), and t. For pure TE (E_y, H_x, H_z) or TM (H_y, E_x, E_z) modes excitation [18], the orientation direction of LC can be along the z-axis (LC-z) or y-axis (LC-y). The relative permittivity tensor ε_{LC} of LC can be expressed in the following forms:

$$\varepsilon_{LC} = \begin{bmatrix} \varepsilon_{xx} & & \\ & \varepsilon_{yy} & \\ & & \varepsilon_{zz} \end{bmatrix}. \tag{1}$$

ε_{xx}, ε_{yy}, and ε_{zz} are the relative dielectric constants of the LC in the x, y, and z directions respectively. For LC-y orientation, ε_{xx}, ε_{yy}, and ε_{zz} are denoted as n_o^2, n_e^2, and n_o^2. For LC-z orientation, ε_{xx}, ε_{yy}, and ε_{zz} are denoted as n_o^2, n_o^2, and n_e^2. Here, n_o and n_e represent the ordinary and extraordinary refractive indices of LC. By incorporating the relative permittivity tensor of LC into Maxwell's curl equations, the decoupled TE and TM modes satisfy the following differential equations:

$$\begin{array}{l} \frac{\partial^2 E_y}{\partial x^2} + k_0^2(\varepsilon_{yy} - n_{eff}^2)E_y = 0 \\ \frac{\partial^2 H_y}{\partial x^2} + k_0^2\left(\varepsilon_{zz} - n_{eff}^2\frac{\varepsilon_{zz}}{\varepsilon_{xx}}\right)H_y = 0 \end{array}. \tag{2}$$

k_0 represents the vacuum wave vector, and n_{eff} denotes the effective refractive index of the waveguide. For TE mode, regardless of the LC orientation, the above formula is always equivalent to an isotropic cladding structure with a refractive index of $\varepsilon_{yy}^{1/2}$. For TM mode, under LC-y orientation, the above formula is also equivalent to an isotropic cladding structure with a refractive index of n_o. For TM mode under LC-z orientation, the ε_{xx} and ε_{zz} are different, there is no equivalent isotropic structure and the anisotropic property should be considered carefully.

The field distribution H_y of the TM mode in each layer can be expressed as:

$$H_{y_{j\pm}} = c_{j\pm} \exp(ik_0 n_{eff} z) \begin{cases} \exp(\pm i\xi_j x) \\ \exp(\pm p_j x) \end{cases}. \tag{3}$$

Where the subscript j denotes the layer number ($j = 1$ refers to the core layer, etc.), while $c_{j\pm}$ represents the complex amplitude of the field in each layer. The field distribution in each layer represents as a combination of transverse (x) and longitudinal (z) field distributions. ξ_j and p_j are the transverse wave vectors, defined as $\xi_j = k_0$ $(n_j^2 - n_{eff}^2)^{1/2}$ and $p_j = k_0$ $(n_{eff}^2 - n_j^2)^{1/2}$. The transverse wave vector of the TM mode in the LC layer is defined as $\xi_{TMLC} = k_0$ $(\varepsilon_{zz} - \varepsilon_{zz}/\varepsilon_{xx}n_{eff}^2)^{1/2}$ and $p_{TMLC} = k_0$ $(\varepsilon_{zz}/\varepsilon_{xx}n_{eff}^2 - \varepsilon_{zz})^{1/2}$. The transverse field distribution for each

layer can be further expressed as:

$$
H_y = \begin{cases}
A\exp(i\xi_1(x+s(z))) + B\exp(-i\xi_1(x+s(z))) & -d(z)-s(z) \le x \le -s(z) \\
C\exp(-p_2(x+s(z))) + D\exp(p_2(x+s(z))) & -s(z) \le x \le 0 \\
E\exp(-p_0(x+d(z)+s(z))) + F\exp(p_0(x+d(z)+s(z))) & -d(z)-s(z)-t \le x \le -d(z)-s(z) \\
G\exp(i\xi_3 x) & x \ge 0 \\
O\exp(p_{TMLC}(x+d(z)+s(z)+t)) & x \le -d(z)-s(z)-t
\end{cases}
$$

$$(4)$$

A-O represents the complex amplitude. Considering the continuity of the magnetic field H_y and the electric field E_z at each interface, eight linear equations can be obtained, which can be written in matrix form as follows:

$$
\mathbf{Mv} =
\begin{bmatrix}
1 & 1 & -1 & -1 & 0 & 0 & 0 & 0 \\
\frac{i\xi_1}{n_1^2} & \frac{-i\xi_1}{n_1^2} & \frac{p_2}{n_2^2} & \frac{-p_2}{n_2^2} & 0 & 0 & 0 & 0 \\
\exp(-i\xi_1 d(z)) & \exp(i\xi_1 d(z)) & 0 & 0 & -1 & -1 & 0 & 0 \\
\frac{i\xi_1 \exp(-i\xi_1 d(z))}{n_1^2} & \frac{-i\xi_1 \exp(-i\xi_1 d(z))}{n_1^2} & 0 & 0 & \frac{p_0}{n_0^2} & \frac{-p_0}{n_0^2} & 0 & 0 \\
0 & 0 & \exp(-p_2 s(z)) & \exp(p_2 s(z)) & 0 & 0 & -1 & 0 \\
0 & 0 & \frac{-p_2 \exp(-p_2 s(z))}{n_2^2} & \frac{p_2 \exp(p_2 s(z))}{n_2^2} & 0 & 0 & -\frac{i\xi_3}{n_3^2} & 0 \\
0 & 0 & 0 & 0 & \exp(p_0 t) & \exp(-p_0 t) & 0 & -1 \\
0 & 0 & 0 & 0 & \frac{-p_0 \exp(p_0 t)}{n_0^2} & \frac{p_0 \exp(-p_0 t)}{n_0^2} & 0 & \frac{-p_{TMlc}}{\varepsilon_{zz}}
\end{bmatrix}
\begin{bmatrix}
A \\ B \\ C \\ D \\ E \\ F \\ G \\ O
\end{bmatrix} = 0.
$$

$$(5)$$

Where the $\mathbf{M}$ is an 8×8 matrix containing coefficients associated with complex amplitudes, and $\mathbf{v}$ is an 8×1 column vector composed of eight complex amplitudes A-O that need to be determined. According to linear algebra, only when the determinant of the matrix $\mathbf{M}$ is equal to 0, there exists non-zero solutions for these complex amplitudes. Solving this condition of determinant being zero can give the value of effective refractive index $n_{eff}(z)$. Due to the presence of a prism, the $n_{eff}(z)$ becomes complex and can be expressed as $n_{eff}(z) = n_{eff1}(z) + i n_{eff2}(z)$, where $n_{eff2}(z)$ represents leakage. Furthermore, the complex amplitude coefficient $G(z)$ of the field leaking into the prism can be calculated using the following formula:

$$
G(z) = m\mathbf{M}_{r7}.
$$

$$(6)$$

Where m is an arbitrary constant, $\mathbf{M}_{r7}$ is a cofactor of matrix $\mathbf{M}$, and r is an arbitrary row number, ranging from 1 to 8. Combining the longitudinal field distribution at different z positions, the Ω^* of the SEEOR coupling structure can be obtained by:

$$
\Omega^*(z) = G(z)\exp\left(ik_0 \int_{z_1}^{z} n_{eff}(\zeta)d\zeta\right).
$$

$$(7)$$

Introducing the expression of $n_{eff}(z)$ into the above formula, Ω^* can be rewritten in terms of amplitude and phase multiplication:

$$
\Omega^*(z) = |\Omega^*(z)|\exp(i\varphi(\Omega^*(z))) = \left|G(z)\exp\left(-k_0 \int_{z_1}^{z} n_{eff2}(\zeta)d\zeta\right)\right|\exp\left(i(\varphi(G(z)) + k_0 \int_{z_1}^{z} n_{eff1}(\zeta)d\zeta)\right).
$$

$$(8)$$

The amplitude distribution of Ω^* represents its profile. As evident from Eq. (8), n_{eff2} predominantly influences the profile distribution of Ω^*, whereas n_{eff1} primarily impacts the phase distribution of Ω^*. As a result, a mode field distribution that perfectly matches the above coupling structure is obtained. If this field distribution is incident, its coupling efficiency can

theoretically reach 100%. For any incident beam e_{in}, the actual coupling efficiency can be derived by the overlap integral between e_{in} and Ω^*:

$$\eta = \frac{|\langle e_{in}|\Omega^*\rangle|^2}{|\langle e_{in}|e_{in}^*\rangle||\langle\Omega|\Omega^*\rangle|}. \tag{9}$$

The denominator represents the inner product between the incident beam e_{in} and Ω^* with respect to themselves, and the numerator's expression in Eq. (9) is as follows:

$$|\langle e_{in}|\Omega^*\rangle|^2 = \left(\int_0^{z_1}|e_{in}||\Omega^*|\cos(\varphi(e_{in})-\varphi(\Omega^*))dz\right)^2 + \left(\int_0^{z_1}|e_{in}||\Omega^*|\sin(\varphi(e_{in})-\varphi(\Omega^*))dz\right)^2 \tag{10}$$

From the calculation expression for coupling efficiency, it is apparent that two factors affect the actual coupling efficiency. The first factor is the similarity of contour between the incident beam and Ω^*, while the second factor is the phase difference. Consequently, for any incident beam, the optimal coupling structure can be obtained by optimizing the waveguide structure parameters.

3. Design and performance analysis of SEEOR coupling structure

In this section, a SEEOR for TM mode with *LC-z* orientation was designed and optimized. The working wavelength is set to 1550 nm. The high refractive index glass (H-Zlaf90) with a refractive index of 1.946 is used as the coupling prism. The nitrogen-doped silicon oxide (SION) with a refractive index of 1.845 is used as the core layer, and the silicon dioxide (SiO$_2$) with a refractive index of 1.455 is used as the gap layer. A 30 nm alignment layer with a refractive index of 1.5 is placed in between the waveguide core and LC cladding. The LC material is 5CB [19], with ordinary and extraordinary refractive indices of 1.511 and 1.661.

For beam steering applications, the primary goal of designing the thickness of waveguide core layer is to ensure the stable transmission of TM$_0$ mode in the core layer during the modulation process of the LC layer. Figure 2(a) illustrates the relationship between the effective refractive index of the waveguide mode and the core layer thickness under two LC modulation condition. It indicates that the thickness of core layer should between 360 nm to 840 nm for a single TM$_0$ mode transmission. The thickness of the core layer in this design is determined to be 579 nm.
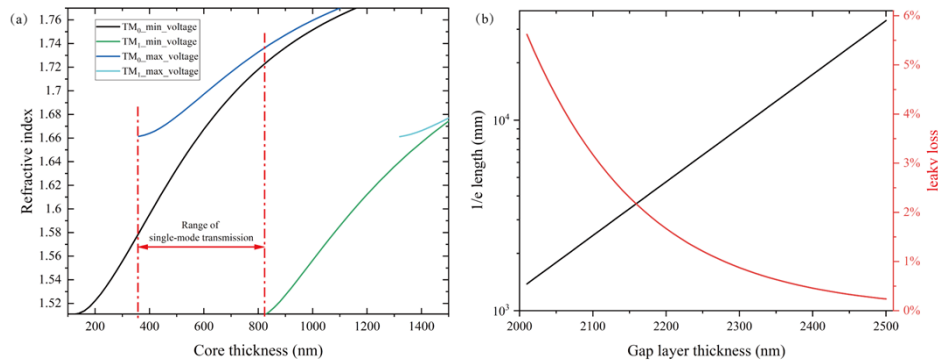

Fig. 2. (a) The effective refractive index of TM$_0$ (black solid line) and TM$_1$ (green solid line) without applied voltage, and TM$_0$ (blue solid line) and TM$_1$ (cyan solid line) with maximum voltage at different core thicknesses (b) The length of the 1/e amplitude decay of the core layer (black solid line) and the energy loss caused by a 40 mm leakage transmission (red solid line) at different gap layer thicknesses.

At horizontal beam steering region, the gap layer must be thick enough to minimize the leakage loss from core layer to prism. The leakage strength can be evaluated by the propagation length

at which the amplitude of core layer decays to 1/e due to the leakage. The solid black line in Fig. 2(b) depicts the variations of this length for different gap layer thicknesses. For a fixed 40 mm transmission length, the percentage of energy loss caused by the leakage is shown by the solid red line in Fig. 2(b). Consequently, the gap layer thickness is set to 2400 nm, and for a transmission length of 40 mm, the energy loss caused by leakage does not exceed 0.5%.

For Gaussian beam incidence, the field distribution at the interface between prism and gap layer can be described by:

$$e_{in} = \exp\left(-\left(\frac{z - z_{00}}{w_0}\right)^2\right)\exp(-ik_0 n_3 \sin(\alpha)z). \tag{11}$$

Where w_0 is the waist radius of the Gaussian beam, α is the incident angle at the interface and z_{00} is the location of waist center. In order to achieve 100% coupling efficiency, the thickness distribution of gap layer and core layer in the input coupling area is optimized. Figure 3(a) illustrates the optimized thickness distribution of the core and gap layers. The optimized core layer thickness was changed from 577.4 nm to 579 nm with an almost linear distribution. In contrast, the gap layer features a non-linear distribution, with the thickness steadily increasing from 620 nm to 2400 nm. This output field distribution Ω^* matches perfectly with the Gaussian beam distribution, ensuring the realization of 100% coupling efficiency.
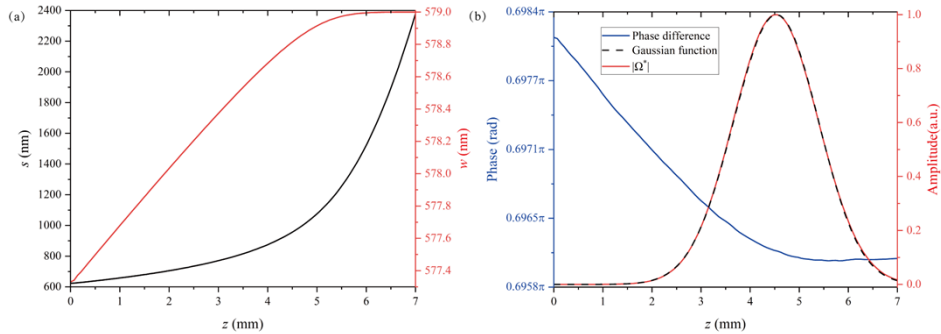

Fig. 3. (a) The distribution of the core layer (red solid line) and the gap layer (black solid line) under the optimal coupling condition. (b) Phase difference distribution between the Gaussian beam and Ω^*(blue solid line), the Gaussian function distribution (black dashed line), and the $|\Omega^*|$ distribution (red solid line)

In addition, we compared the differences between considering anisotropy and isotropic approximation to show the importance of including the anisotropy in the model. To apply an assumed isotropic approximation of LC, the refractive index of LC is set to be isotropic and its numerical value is calculated by $((2n_o^2 + n_e^2)/3)^{1/2}$, which is the average refractive index of LC. Under the same optimal coupling waist radius, Fig. 4(a) shows the comparison of the optimum gap profiles with two different types of LC's Δn (n_e-n_o): 0.15 and 0.4. All other waveguide material parameters are the same except for the difference in LC's Δn. Correspondingly, Fig. 4(b) shows the comparison of the optimum core profiles. It can be seen that there is a difference in the optimal profiles obtained using the two methods. The larger the Δn of the LC, the more significant the difference in the results obtained by the two methods.

Considering the small variation in the core layer thickness, we further analyzed the coupling efficiency under uniform core layer thickness. Figure 5(a) presents the comparison of the $|\Omega^*|$ under a 579 nm uniform core layer thickness and the optimal core layer distribution. The $|\Omega^*|$ distribution under the uniform core layer demonstrates virtually no difference when compared to the optimal core layer distribution. Figure 5(b) illustrates the phase difference distribution
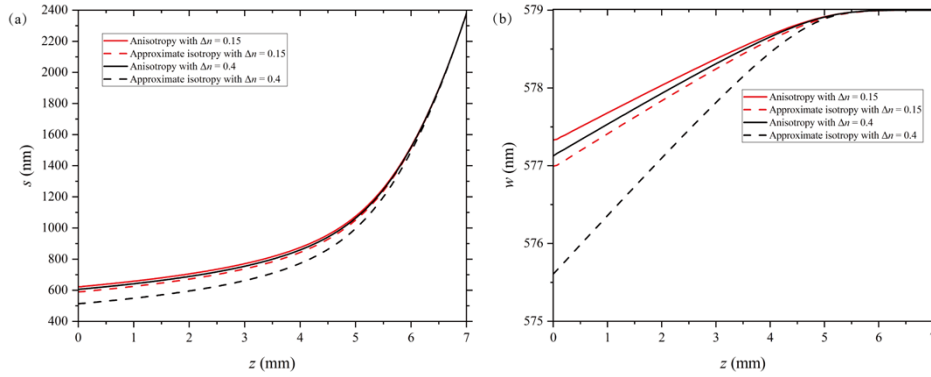
Fig. 4. Comparison of the optimum profiles for considering the anisotropy and approximate isotropy. (a) The optimum gap profile under anisotropy (red solid line) and the optimum gap profile under approximate isotropy (red dashed line) when the Δn of the LC is 0.15, as well as the optimum gap profile under anisotropy (black solid line) and the optimum gap profile under approximate isotropy (black dashed line) when the Δn of the LC is 0.4. (b) The optimum core profile under anisotropy (red solid line) and the optimum core profile under approximate isotropy (red dashed line) when the Δn of the LC is 0.15, as well as the optimum core profile under anisotropy (black solid line) and the optimum core profile under approximate isotropy (black dashed line) when the Δn of the LC is 0.4.

between the Gaussian beam and Ω^*, along with the product distribution between the Gaussian beam contour and $|\Omega^*|$. In comparison to the optimal core layer, the phase change from $z = 0$ to $z = 2.5$ mm varies from 0.013 π to 1.067 π, suggesting that the approximation of a uniform core layer distribution can result in phase mismatch and diminished coupling efficiency. Nonetheless, the coupling efficiency can still attain 99.3%.
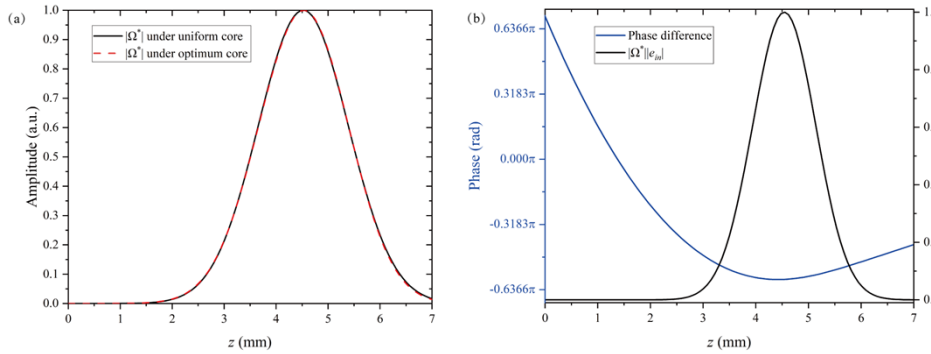

Fig. 5. (a) The distribution of $|\Omega^*|$ under the uniform core layer (black solid line) and the optimal core layer (red dashed line). (b) The phase difference distribution (blue solid line) between the Gaussian beam and Ω^*, as well as the product distribution (black solid line) of the Gaussian beam profile and $|\Omega^*|$

Regarding the thickness distribution of the gap layer, we considered the practical process feasibility and further analyzed the coupling efficiency attainable by a near-linear gap layer prepared using the offset shadow mask approach reported in the literature [20]. Figure 6(a) contrasts the difference between the linear gap layer approximation and the optimal gap layer distribution, setting the gap layer thickness at $z = 0$ to be 400 nm and at $z = 7$ mm to be 2400 nm.

Concurrently, $|\Omega^*|$ and the corresponding optimal Gaussian beam profile are shown in Fig. 6(b), a coupling efficiency of 94.8% can be achieved.
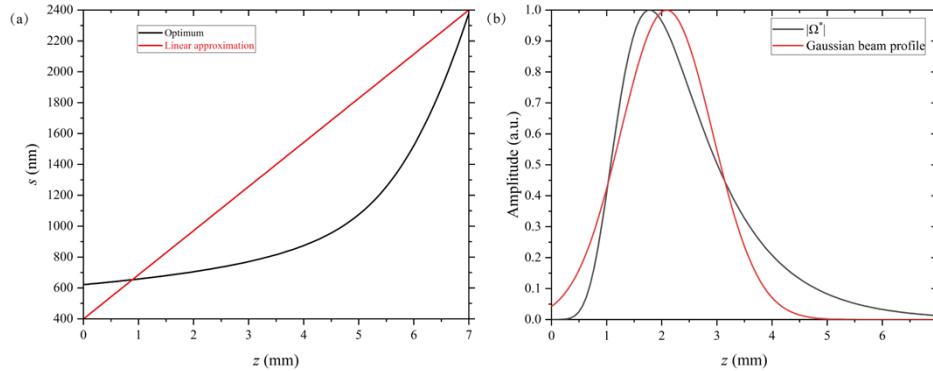

Fig. 6. (a) Linear gap layer approximation (red solid line) and optimal gap layer distribution (black solid line). (b) The distributions of the Gaussian beam profile (red solid line) and $|\Omega^*|$ (black solid line).

In addition, the effects of waist radius, center position, and incident angle of Gaussian beam on coupling efficiency are analyzed. Figure 7(a) illustrates the coupling efficiency variations with respect to waist radius and center position. For a coupling efficiency over 90%, the allowable deviation of waist radius and center position are 0.66 mm and 0.58 mm respectively. Figure 7(b) portrays the coupling efficiency at different incident angles, with the full width at half maximum (FWHM) of the incident angle being -0.02° ~ 0.021°. This result indicates that the coupling structure is extremely sensitive to the incident angle and requires precise adjustments during the experimental process to achieve efficient coupling.
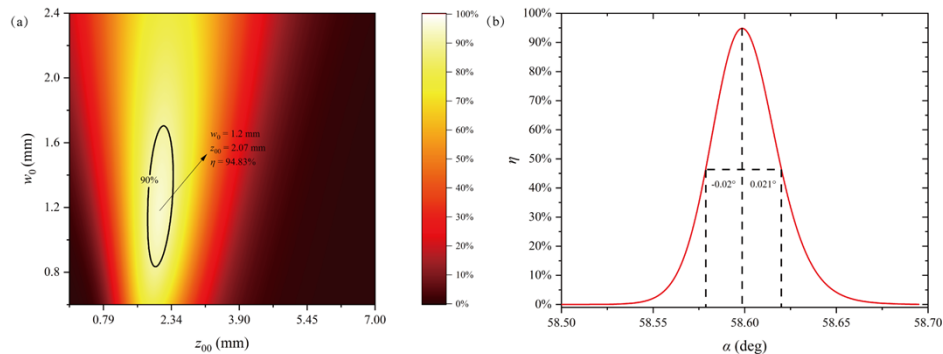

Fig. 7. (a) The relationship between coupling efficiency and the beam waist radius and center position of the input beam. (b) The relationship between coupling efficiency and incident angle.

4. Experiment

The fabrication process of the SEEOR device is shown in Fig. 8. The coupling prism has dimensions of 39 mm in length, 25 mm in width, 5 mm in thickness, and a 61° wedge angle. Moreover, a conductive film (ITO) with a thickness of 10 nm to 20 nm covers the upper surface of the prism, which corresponds to the horizontal beam steering and the coupling output regions. A near-linearly distributed SiO2 gap layer was deposited onto the coupling prism using the deviated

shadow mask technique. Following this, a uniform SiON core layer was formed on the base through sputtering. An alignment layer was then spin-coated onto the core layer and subjected to orientation treatment. Subsequently, the cell was assembled by placing conventional spacers of thickness 6.5 μm using UV curable glue. Upon assembly, 5CB was introduced into the waveguide through capillary action, aligning the molecules along the propagation direction. Ultimately, we obtained a compact device as displayed in Fig. 8(f).
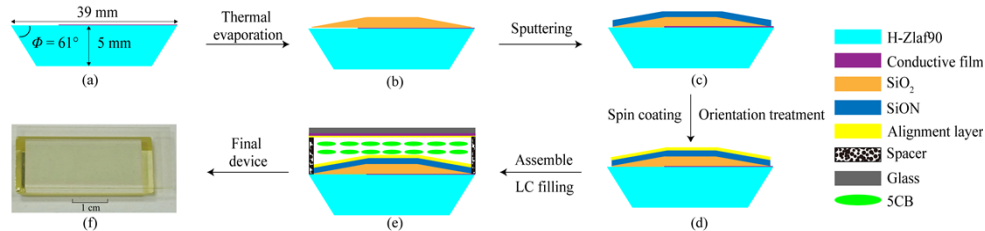
Fig. 8. Steps for fabricating the SEEOR device: (a) cleaned coupling prism substrate, (b) preparing a linear SiO2 gap layer through thermal evaporation, (c) preparing SiON core layer through sputtering, (d) spin-coating the alignment layer and performing orientation treatment, (e) assembling the glass cover plate to form the cell and filling with 5CB LC, (f) actual device sample image.

The coupling efficiency of the SEEOR device was measured using the setup depicted in Fig. 9. A 1550 nm linearly polarized TEM$_{00}$ mode laser was used as the light source. The waist radius can be continuously adjusted by a beam expander from 0.25 mm to 1.25 mm. A half-wave plate was used to rotate the polarization direction to generate the TM polarized light. The sample was placed on a four-axis adjustment stage, and a CCD camera was utilized to record the light propagation and steering process by collecting the scattered light from the waveguide. Finally, a power meter was utilized to measure the energy associated with coupling efficiency.
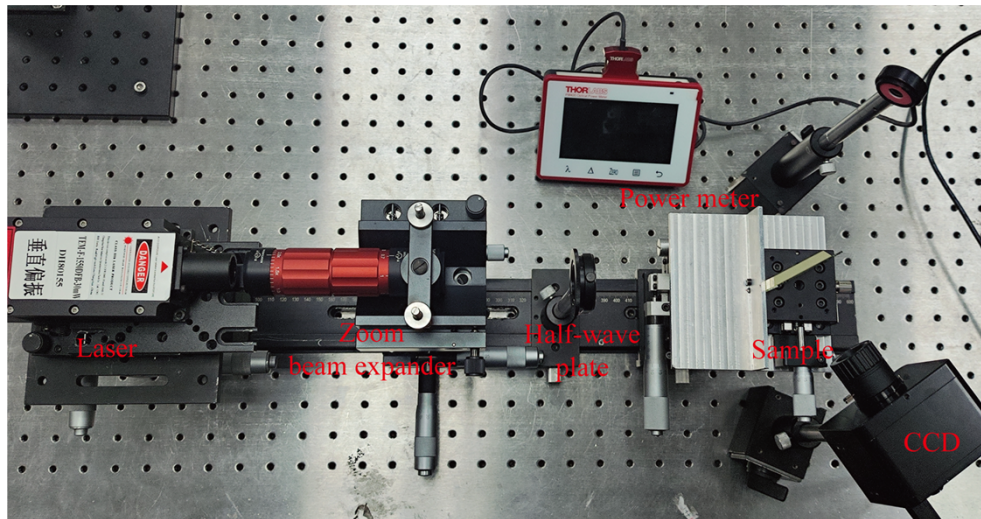

Fig. 9. Optical path diagram for coupling efficiency testing.

Figure 10(a) illustrates the light propagation process in the device. The input light (I_{in}) is partially reflected by the surface of the prism (I_r), then entered into the prism. Most of the light (red solid line with arrow) is coupled into the core layer and propagates to the output coupling

region. During transmission, the scattering caused by LC itself and the surface roughness of the thin film, as well as the slight absorption of the waveguide material, leads to energy loss. Finally, it leaks into the prism with 100% output coupling efficiency and then is output through the prism (I_{out}). The light (red dashed line with arrow) that is not coupled into the core layer will propagate in the prism in the form of total reflection and output from the end face of the prism (I_2). By carefully adjusting the incident angle and coupling position of the incident beam, we can get the optimum coupling when I_2 reached its minimized value ($I_2{}^{min}$), which is found, independently, to correspond to a maximum in the waveguide output (I_{out}). Then, keeping the incident angle fixed, slightly moving the coupling position until the I_{out} disappears and the I_2 reached its maximum value ($I_2{}^{max}$), shown in Fig. 10(b). The incident beam deviates significantly from the optimal incident center position, resulting in a coupling efficiency of 0.
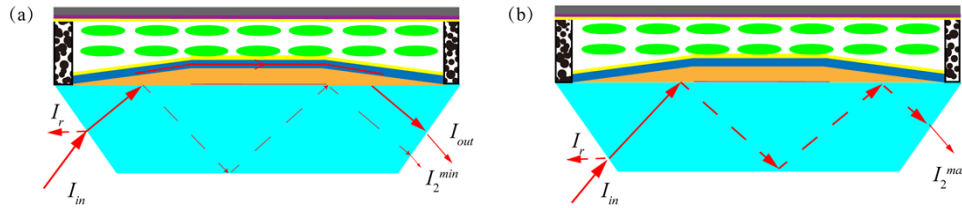

Fig. 10. Schematic diagram of the main beam distribution. (a) Optimal coupling state. (b) No coupling state.

The values of main beam energy under these two states are shown in Table 1. The prism coupler's input coupling efficiency can be related simply to the measured I_2 intensities by:

$$\eta = \frac{I_2{}^{max} - I_2{}^{min}}{I_2{}^{max}}. \tag{12}$$

Table 1. Main beam energy under optimum coupling and no coupling

	I_{in}	I_r	I_{out}	I_2
Optimum coupling state	7.73 mW	0.79 mW	2.01 mW	0.55 mW
No coupling state	7.73 mW	0.79 mW	-	6.20 mW

The input coupling efficiency calculated by using I_2 under two states is 91%. Besides using I_2, we also consider the propagation process of the beam from I_{in} to I_{out}. The energy of the beam entering the prism depends on the input energy multiplied by the transmittance (one minus the reflectance (I_r/I_{in})). Under the optimal coupling state, this portion of beam is coupled into the waveguide with coupling efficiency η. The propagation loss (PL) is calculated by using the method reported in Ref. [21]. The result in Fig. 11 shows that the PL coefficient is 1.49 dB/cm, and the device has a total PL of approximately 4.47 dB. The beam leaking to the prism is multiplied by the transmittance to obtain I_{out}. The input coupling efficiency can also be related to the measured I_{in}, I_r, I_{out}, and PL by:

$$\eta = \frac{I_{out}}{I_{in}\left(1 - \frac{I_r}{I_{in}}\right)^2 10^{-\frac{PL}{10}}}. \tag{13}$$

The calculated coupling efficiency is 90.3%, which is almost consistent with the result obtained by utilizing Eq. (12). Taking into account various experimental imperfections (Deviations in the thickness and refractive index of the waveguide layers, Gaussian beam noise), this efficiency is deemed to be in reasonable agreement with the theoretical value of 94.8%.
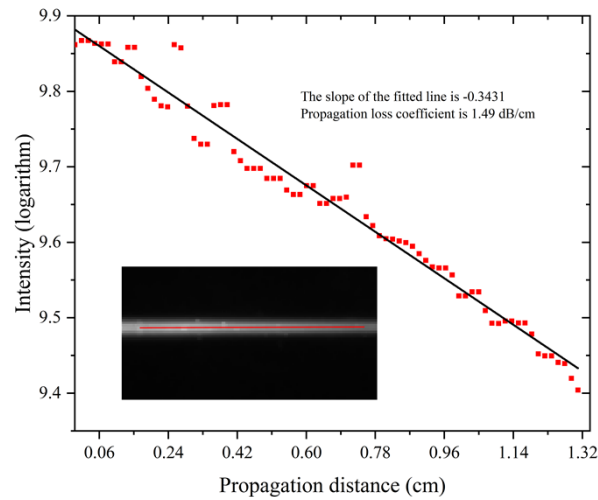
Fig. 11. An image and "intensity (logarithm) vs. distance" plot of a guided intensity of 1550 nm light as it propagates through the LC cladding waveguide.

In addition to testing the coupling efficiency under the optimal coupling conditions, we also evaluated the device performance when deviating from the optimal coupling conditions. First, we measured the optimal coupling efficiency for different beam waists. The result in Fig. 12(a) shows that an upward deviation is less serious in practice than a downward deviation. Then, we fixed the waist size at the optimal parameters and examined how the beam center position and incident angle affected the coupling efficiency. Considering the requirement for Gaussian incident angle in Section 3 and the prism's wedge angle, the Gaussian beam is refracted into the prism at an incidence angle of approximately 4.7°. In accordance with Snell's law of refraction, the beam center position change at the film-prism interface is about 2.06 times the sample position deviation, and the sample rotation angle change is about n_3 times the coupling angle change. The experimental results are illustrated in Fig. 12(b) and Fig. 12(c). These results demonstrate good consistency with the theoretical prediction. After fitting the coupling angle data with a Gaussian function, the measured angular full width at half maximum (FWHM) is found to be $\pm 0.0205°$.
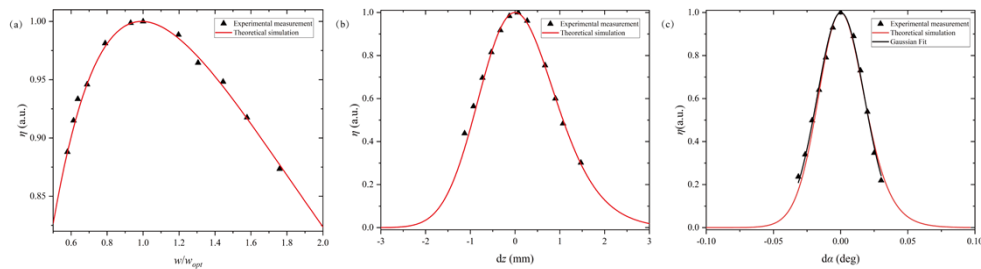

Fig. 12. Comparison of theoretical and experimental results. (a) Theoretical curve (red solid line) of normalized coupling efficiency as a function of beam waist and experimental data (black triangles). (b) Theoretical curve (red solid line) of normalized coupling efficiency as a function of beam center position and experimental data (black triangles). (c) Theoretical curve (red solid line) of normalized coupling efficiency as a function of incident angle, experimental data (black triangles), and Gaussian fit (black solid line) of experimental data.

At the same time, the beam steering characteristics of the device were also tested. In the optimal coupling state, we utilized a CCD camera to document the deflection of the beam within the waveguide as well as the output beam position from the prism, under both voltage-applied and voltage-free conditions. To capture the output beam, we substituted the power meter probe in Fig. 8 with an imaging card and recorded the beam's position by imaging the beam on the card. Figure 13 illustrates the observed beam deflection. The detail of the internal beam deflection in waveguide is shown in Visualization 1.
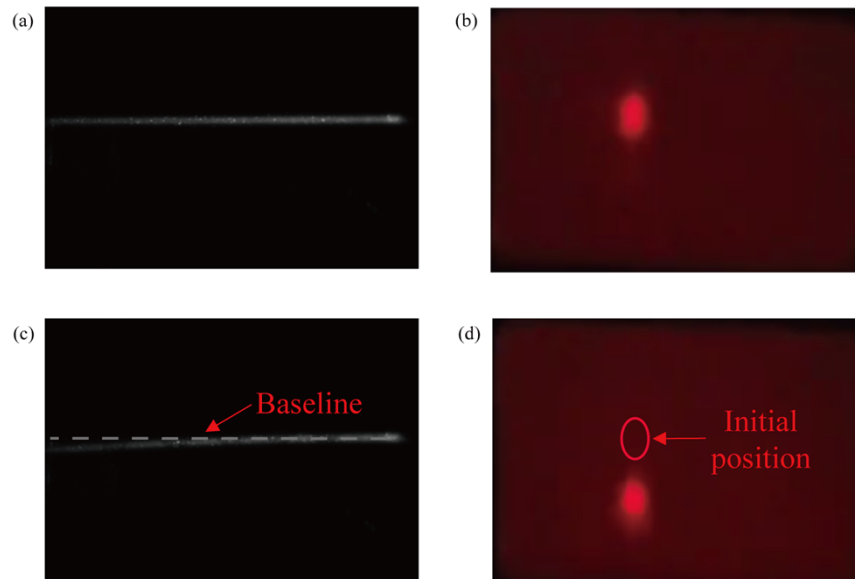

Fig. 13. (a) Internal beam propagation in the waveguide under the voltage-free condition. (b) Output beam position under the voltage-free condition. (c) Internal beam propagation in the waveguide under the voltage-applied condition (see Visualization 1). (d) Output beam position under the voltage-applied condition.

5. Conclusion

This article investigates the SEEOR coupling structure with anisotropic LC cladding through theory, simulation, and experiments. The Ω^* distribution of TM mode under *LC-z* orientation mode was obtained for accurate coupling efficiency analysis. The optimal coupling structure of SEEOR for Gaussian beam is given. Further considering the manufacture implementation method, a simplified prism coupling structure that can achieve coupling efficiency better than 94% was proposed. The results show that the coupling structure is relatively insensitive to the Gaussian beam profile but extremely sensitive to the incident angle, and the FWHM of the coupling angle is about ±0.02°. Finally, we prepared the device and carried out performance testing. The experimental results were consistent with theoretical calculations. These research results are of great significance for the development and application of SEEOR.

References

1. E. Betzig and J. K. Trautman, "Near-field optics: microscopy, spectroscopy, and surface modification beyond the diffraction limit," Science **257**(5067), 189–195 (1992).
2. G. W. Kattawar and G. N. Plass, "Time of flight lidar measurements as an ocean probe," Appl. Opt. **11**(3), 662–666 (1972).
3. J. W. Hair, C. A. Hostetler, A. L. Cook, D. B. Harper, R. A. Ferrare, T. L. Mack, W. Welch, L. R. Izquierdo, and F. E. Hovis, "Airborne high spectral resolution lidar for profiling aerosol optical properties," Appl. Opt. **47**(36), 6734–6752 (2008).
4. D. Faklis and G. M. Morris, "Diffractive optics technology for display applications," Proc. SPIE **2407**, 57–61 (1995).
5. R. A. Meyer, "Optical beam steering using a multichannel lithium tantalate crystal," Appl. Opt. **11**(3), 613–616 (1972).
6. G. D. Reddy and P. Saggau, "Fast three-dimensional laser scanning scheme using acousto-optic deflectors," J. Biomed. Opt. **10**(6), 064038 (2005).
7. J. Cheng and C.-L. Chen, "Adaptive beam tracking and steering via electrowetting-controlled liquid prism," Appl. Phys. Lett. **99**(19), 191108 (2011).
8. D. Resler, D. Hobbs, R. Sharp, L. Friedman, and T. Dorschner, "High-efficiency liquid-crystal optical phased-array beam steering," Opt. Lett. **21**(9), 689–691 (1996).
9. D. Engström, M. J. O'Callaghan, C. Walker, and M. A. Handschy, "Fast beam steering with a ferroelectric-liquid-crystal optical phased array," Appl. Opt. **48**(9), 1721–1726 (2009).
10. J. Kim, C. Oh, M. J. Escuti, and S. Serati, "Wide-angle nonmechanical beam steering using thin liquid crystal polarization gratings," in *Advanced wavefront control: methods, devices, and applications VI, Proc. SPIE* 7093, 709302 (2008).
11. J. Kim, M. N. Miskiewicz, S. Serati, and M. J. Escuti, "Nonmechanical laser beam steering based on polymer polarization gratings: design optimization and demonstration," J. Lightwave Technol. **33**(10), 2068–2077 (2015).
12. M. Ziemkiewicz, S. R. Davis, S. D. Rommel, D. Gann, B. Luey, J. D. Gamble, and M. Anderson, "Laser-based satellite communication systems stabilized by non-mechanical electro-optic scanners," in *Airborne Intelligence, Surveillance, Reconnaissance (ISR) Systems and Applications XIII, Proc. SPIE* 9828, 31–42 (2016).
13. J. A. Frantz, J. D. Myers, R. Y. Bekele, C. M. Spillmann, J. Naciri, J. S. Kolacz, H. Gotjen, L. B. Shaw, J. S. Sanghera, and B. Sodergren, "Non-mechanical beam steering in the mid-wave infrared," in *Advanced Optics for Defense Applications: UV through LWIR II, Proc. SPIE* 10801, 206–212 (2017).
14. J. A. Frantz, J. D. Myers, R. Y. Bekele, C. M. Spillmann, J. Naciri, J. Kolacz, H. G. Gotjen, V. Q. Nguyen, C. C. McClain, and L. B. Shaw, "Chip-based nonmechanical beam steerer in the midwave infrared," J. Opt. Soc. Am. B **35**(12), C29–C37 (2018).
15. R. Ulrich, "Optimum excitation of optical surface waves," J. Opt. Soc. Am. **61**(11), 1467–1477 (1971).
16. J. Revelli, "Enhancement of prism coupling efficiency in uniform optical waveguides: a correction," J. Appl. Phys. **52**(5), 3185–3189 (1981).
17. J. F. Revelli, "Mode analysis and prism coupling for multilayered optical waveguides," Appl. Opt. **20**(18), 3158–3167 (1981).
18. J. Kołacz, H. G. Gotjen, R. Y. Bekele, J. D. Myers, J. A. Frantz, M. Ziemkiewicz, and C. M. Spillmann, "Propagating transverse electric and transverse magnetic modes in liquid crystal-clad planar waveguides," Liq. Cryst. **47**(4), 531–539 (2020).
19. V. Tkachenko, G. Abbate, A. Marino, F. Vita, M. Giocondo, A. Mazzulla, F. Ciuchi, and L. D. Stefano, "Nematic Liquid Crystal Optical Dispersion in the Visible-Near Infrared Range," Mol. Cryst. Liq. Cryst. **454**(1), 263/[665] (2006).
20. J. D. Myers, J. A. Frantz, C. M. Spillmann, R. Y. Bekele, J. Kolacz, H. Gotjen, J. Naciri, B. Shaw, and J. S. Sanghera, "Refractive waveguide non-mechanical beam steering (NMBS) in the MWIR," in *Photonic Instrumentation Engineering V, Proc. SPIE* 10539, 47–53 (2018).
21. Y. Okamura, S. Yoshinaka, and S. Yamamoto, "Measuring mode propagation losses of integrated optical waveguides: a simple method," Appl. Opt. **22**(23), 3892–3894 (1983).